

Dynamical analysis, geometric control and digital hardware implementation of a complex-valued laser system with a locally active memristor

Yi-Qun Li(李逸群), Jian Liu(刘坚), Chun-Biao Li(李春彪),Zhi-Feng Hao(郝志峰), and Xiao-Tong Zhang(张晓彤)
Citation: Chin. Phys. B, 2023, 32 (**8**): 080503. DOI: 10.1088/1674-1056/acd68b
Journal homepage: http://cpb.iphy.ac.cn; http://iopscience.iop.org/cpb
What follows is a list of articles you may be interested in

Diffusive field coupling-induced synchronization between neural circuits under energy balance

Ya Wang(王亚), Guoping Sun(孙国平), and Guodong Ren(任国栋)
Chin. Phys. B, 2023, 32 (**4**): 040504. DOI: 10.1088/1674-1056/ac7bff

Extremely hidden multi-stability in a class of two-dimensional maps with a cosine memristor

Li-Ping Zhang(张丽萍), Yang Liu(刘洋), Zhou-Chao Wei(魏周超), Hai-Bo Jiang(姜海波), Wei-Peng Lyu(吕伟鹏), and Qin-Sheng Bi(毕勤胜)
Chin. Phys. B, 2022, 31 (**10**): 100503. DOI: 10.1088/1674-1056/ac7294

A class of two-dimensional rational maps with self-excited and hidden attractors

Li-Ping Zhang(张丽萍), Yang Liu(刘洋), Zhou-Chao Wei(魏周超),Hai-Bo Jiang(姜海波), and Qin-Sheng Bi(毕勤胜)
Chin. Phys. B, 2022, 31 (**3**): 030503. DOI: 10.1088/1674-1056/ac4025

A novel class of two-dimensional chaotic maps with infinitely many coexisting attractors

Li-Ping Zhang(张丽萍), Yang Liu(刘洋), Zhou-Chao Wei(魏周超), Hai-Bo Jiang(姜海波), Qin-Sheng Bi(毕勤胜)
Chin. Phys. B, 2020, 29 (**6**): 060501. DOI: 10.1088/1674-1056/ab8626

Multi-stability involved mixed bursting within the coupled pre-Bötzinger complex neurons

Zijian Wang(王子剑), Lixia Duan(段利霞), Qinyu Cao(曹秦禹)
Chin. Phys. B, 2018, 27 (**7**): 070502. DOI: 10.1088/1674-1056/27/7/070502

Dynamical analysis, geometric control and digital hardware implementation of a complex-valued laser system with a locally active memristor

Yi-Qun Li(李逸群)[1], Jian Liu(刘坚)[1,†], Chun-Biao Li(李春彪)[2,3], Zhi-Feng Hao(郝志峰)[1], and Xiao-Tong Zhang(张晓彤)[1]

[1] *School of Mathematical Sciences, University of Jinan, Jinan* 250022, *China*
[2] *School of Artificial Intelligence, Nanjing University of Information Science and Technology, Nanjing* 210044, *China*
[3] *Collaborative Innovation Center on Forecast and Evaluation of Meteorological Disasters, Nanjing University of Information Science and Technology, Nanjing* 210044, *China*

(Received 29 March 2023; revised manuscript received 16 May 2023; accepted manuscript online 18 May 2023)

In order to make the peak and offset of the signal meet the requirements of artificial equipment, dynamical analysis and geometric control of the laser system have become indispensable. In this paper, a locally active memristor with non-volatile memory is introduced into a complex-valued Lorenz laser system. By using numerical measures, complex dynamical behaviors of the memristive laser system are uncovered. It appears the alternating appearance of quasi-periodic and chaotic oscillations. The mechanism of transformation from a quasi-periodic pattern to a chaotic one is revealed from the perspective of Hamilton energy. Interestingly, initial-values-oriented extreme multi-stability patterns are found, where the coexisting attractors have the same Lyapunov exponents. In addition, the introduction of a memristor greatly improves the complexity of the laser system. Moreover, to control the amplitude and offset of the chaotic signal, two kinds of geometric control methods including amplitude control and rotation control are designed. The results show that these two geometric control methods have revised the size and position of the chaotic signal without changing the chaotic dynamics. Finally, a digital hardware device is developed and the experiment outputs agree fairly well with those of the numerical simulations.

Keywords: complex-valued chaotic systems, locally active memristor, multi-stability, Hamilton energy, geometric control

PACS: 05.45.Gg, 05.45.Jn, 05.45.Pq **DOI:** 10.1088/1674-1056/acd68b

1. Introduction

In 1960, physicist Maiman invented the first operational ruby laser.[1] Compared with the traditional chaotic systems, laser chaotic systems usually have larger bandwidth, lower attenuation, more complex dynamical behaviors, and greater sensitivity to parameter variations,[2,3] so they can be widely used in high-speed remote confidential communications.[4,5] Since the advent of artificial intelligence, much attention has been paid to neuroprosthetics, which aims to develop electronic devices implanted in the brain to repair missing or malfunctioning brain functions due to trauma or diseases. And we know the human brain consists of approximately 86 billion neurons interconnected in a complex way by 100–500 trillion synapses to perform computational, cognition, and memory tasks,[6] which means that the study of artificial neurons is one of the key researches in neuroprosthetic technology. Electronic approaches for artificial neuron models have been studied for decades.[7,8] Technology has greatly matured and multiple neuromorphic computing platforms based on electronic circuitry techniques have been developed. However, inherent limitations of the neuromorphic electronic approach affect the operation of the system, such as low operating speed and limited communication link length. Therefore, photonic approaches to artificial neurons that benefit from the ultra-fast speed and multiplexing and easy integration of optical enabling technologies has emerged. And optical signals exhibit many advantages over their electronic counterparts like they consume less energy per bit, have a greater bandwidth density per wire, and display lower crosstalk between multiplexed channels. Even, some laser devices exhibit multiple behaviors also observed in neurons, such as excitability[9,10] and complex nonlinear dynamics.[11,12] And lasers-based artificial neurons have been designed and investigated.[13,14] As a classically chaotic system, the Lorenz laser system was used in artificial neural networks.[15,16] It is important to note that both in terms of information carrying capacity and the diversity of dynamical behaviors, the complex-valued chaotic system clearly outperforms the real-valued chaotic system.[17,18] Therefore, the optical complex-valued neural network is designed.[19,20]

On the other hand, the synapse is a crucial element in biological neural networks, which allowed electrical signals to pass from one neuron to the next via biochemical reactions and activate it. But a simple electronic equivalent has been absent. This complicates the development of hardware that imitates biological architectures in the nervous system. Until the memristor was proposed in 1971,[21] it has drawn significant interest in the fields of neuromorphic circuits because it has some interesting properties (such as the pinched hysteresis loop

[†]Corresponding author. E-mail: ss_liuj@ujn.edu.cn, liujian1990@163.com

© 2023 Chinese Physical Society and IOP Publishing Ltd

current–voltage characteristic, the switching characteristic and the variable resistive property with memory[22,23]). Nonvolatile memristor is a kind of natural memory, which is one of the most suitable circuit components for connecting synaptic weights in neural networks.[24] Therefore, nonvolatile memristors are often used to simulate synapses.[25,26] In addition, the locally active function of the memristor plays a significant role in amplifying signals and maintaining oscillation.[27] So a locally active memristor with non-volatile memory is introduced into the complex-valued Lorenz laser, and complex dynamical behaviors of the memristive laser are uncovered therein, such as numerous oscillation patterns and coexisting multi-stable patterns.

The transmission of information between neurons takes the form of electrical signals. To make signals meet the requirements of artificial devices, they are often controlled geometrically, including amplitude control,[28] offset control,[29,30] and rotation control.[31] To keep the amplitude of chaotic signals within the limits of circuit elements, additional linear transformations are usually required to obtain the desired attractor size.[32] In addition, the broadband characteristics of chaotic signals make it difficult to design linear amplifiers. Therefore, amplitude control without changing chaotic dynamics has a unique role in communication engineering.[33,34] The rotation control of chaotic attractors is a new geometric control, which can achieve peak scaling and offset chaotic attractors simultaneously without changing chaotic dynamics.[35,36] So the rotation control can scale and offset the signal regularly according to the communication needs. However, the above geometric controls are studied in real-valued chaotic systems.[28–36] At present, there is little research on the geometric control of complex-valued chaotic systems.[19] In this article, we study the amplitude control and rotation control of a memristive complex-valued laser chaotic system.

Digital circuit implementation is still a crucial topic because of its advantages of high integration and low power consumption. The circuit implementation in the real field has received a lot of attention up to this point,[28,29] but the digital hardware implementation in the complex field is an open topic.[5] In this research, we construct a complex-valued digital circuit for the physical implementation of the memristive complex-valued Lorenz laser system model and realize the circuit of geometric control of a complex-valued system using ultra-efficient microcontroller and chip.

The main contributions of this article are as follows. Firstly, we design a memristive complex-valued laser system and analyze its dynamical behaviors, including chaotic and quasi-periodic orbits, and extreme multi-stable patterns. Secondly, compared with geometric control in the real-valued chaotic systems,[28–36] this paper focuses on two kinds of geometric control of a complex-valued laser system with a memristor, which can adjust the offset and amplitude of chaotic signals without changing chaotic dynamics. That means the peaks of the signals and the time of the peaks change regularly without dynamics switching. Finally, the circuit of geometric control of a complex-valued laser system has been implemented for the first time, and the output results of the digital hardware implementation are in good accord with those of the numerical simulation.

The rest of this paper is structured as follows. In Section 2, the model of the memristive complex-valued laser system is proposed. In Section 3, the influence of the imaginary parts of the complex parameters on the dynamical behaviors of the laser system is analyzed by using numerical measures. In Section 4, we analyze the extreme multi-stability patterns of the memristive laser system. In Section 5, the amplitude control and rotation control of the memristive laser system is realized. In Section 6, we compare the effect of the introduction of a locally active memristor on the complexity of laser system. In Section 7, digital hardware implementation is given and the experimental results are obtained. The conclusion is given in the last section.

2. Memristor-based complex-valued Lorenz laser model

2.1. Complex-valued Lorenz laser system

Complex-valued Lorenz laser system is defined by

$$\begin{cases} \dot{x} = \sigma(y-x), \\ \dot{y} = -cy + rx - zx, \\ \dot{z} = -bz + \dfrac{1}{2}(\bar{x}y + x\bar{y}), \end{cases} \tag{1}$$

where $x = x^r + \mathrm{j}x^i$, $y = y^r + \mathrm{j}y^i$ are two complex-variables, and z is a real-variable, r and c are complex-parameters defined by $r = r_1 + \mathrm{j}r_2$ and $c = 1 - \mathrm{j}\delta$, σ and b are real-parameters. When $\sigma = 6$, $b = 0.8$, $c = 1 - 0.06\mathrm{j}$, $r = 60 + 0.02\mathrm{j}$ and the initial values are $(2 + 0.02\mathrm{j}, -0.5 + 0.3\mathrm{j}, 5)$, typical phase orbit and corresponding power spectrum of the laser system (1) are shown in Figs. 1(a) and 1(b), respectively. Dense spikes in Fig. 1(b) show system (1) is in a chaotic state. In this case, the corresponding Lyapunov exponents are $(0.72, 0, -0.006, -6.88, -8.63)$ and Kaplan–Yorke dimension is 3.105. A positive Lyapunov exponent and fractal dimension also indicate that system (1) is chaotic.

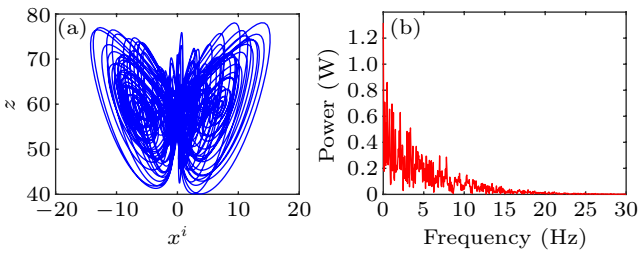


Fig. 1. Chaotic dynamics of the complex-valued Lorenz laser system (1) with $\sigma = 6$, $b = 0.8$, $c = 1 - 0.06\mathrm{j}$, $r = 60 + 0.02\mathrm{j}$ and the initial values $(2 + 0.02\mathrm{j}, -0.5 + 0.3\mathrm{j}, 5)$. (a) The phase trajectory on x^i–z plane and (b) power spectrum.

2.2. A locally active memristor with non-volatile memory

In order to introduce nonlinear feedback into the complex-valued Lorenz laser system (1), we select a voltage-controlled memristor, which is defined by

$$\begin{cases} i = w(u)z, \\ w(u) = u^2 - 3, \\ \dot{u} = -u|u-10| + |u+10| + z, \end{cases} \tag{2}$$

where $w(u)$ is the memductance value, and u is the internal variable related to voltage z. The characteristics of memristor (2) are shown in Fig. 2. The compact hysteresis loop in Fig. 2(a) encircles a smaller area with the increase of frequency and the final area is 0, indicating that memristor (2) meets the fingerprint condition. As can be seen from Fig. 2(b), the POP curve and the horizontal axis have two focal points with negative slope, which indicates that memristor (2) is non-volatile and can keep the data before the power went out. The DC V–I curve of memristor (2) and its near amplification of negative derivative are shown in Figs. 2(c) and 2(d), respectively. The DC V–I curve has a local negative slope in the region $(-20, 0)$, indicating that memristor (2) is a locally active memristor.

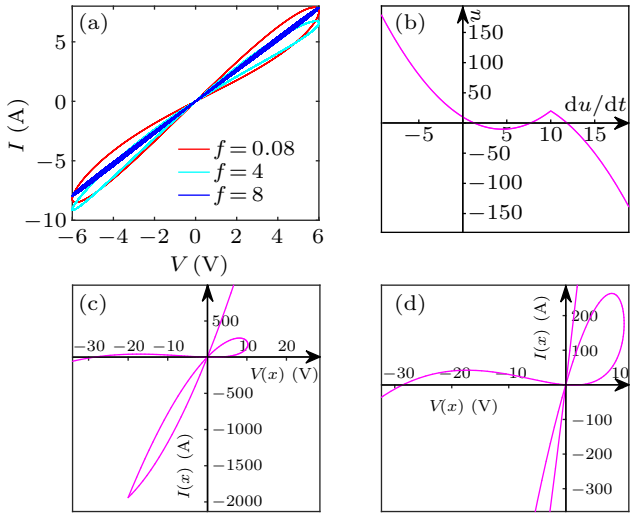


Fig. 2. The features of the voltage-controlled memristor (2). (a) The hysteresis loop; (b) the POP; (c) DC V–I curve; (d) partial enlarged drawing of DC V–I curve.

2.3. Memristive complex-valued Lorenz laser system

Introducing the voltage-controlled memristor (2) to the complex-valued Lorenz laser system (1) can obtain a memristive complex-valued Lorenz laser system

$$\begin{cases} \dot{x} = \sigma(y-x), \\ \dot{y} = -cy + rx - zx, \\ \dot{z} = -b(u^2-3)z + \dfrac{1}{2}(\bar{x}y + x\bar{y}), \\ \dot{u} = -u|u-10| + |u+10| + z, \end{cases} \tag{3}$$

where $x = x^r + \mathrm{j}x^i, y = y^r + \mathrm{j}y^i$ are two complex-variables, z and u are real-variables, σ and b are real-parameters, r and c are complex-parameters defined by $r = r_1 + \mathrm{j}r_2$ and $c = 1 - \mathrm{j}\delta$. The equivalent real-variable form of the laser system (3) is

$$\begin{cases} \dot{x}^r = \sigma(y^r - x^r), \\ \dot{x}^i = \sigma(y^i - x^i), \\ \dot{y}^r = -y^r - x^r z + r_1 x^r - r_2 x^i - \delta y^i, \\ \dot{y}^i = -y^i - x^i z + r_1 x^i + r_2 x^r + \delta y^r, \\ \dot{z} = -b(u^2-3)z + x^r y^r + x^i y^i, \\ \dot{u} = -u|u-10| + |u+10| + z. \end{cases} \tag{4}$$

Let the right of system (4) be zeros, which means

$$\begin{cases} \sigma(y^r - x^r) = 0, \\ \sigma(y^i - x^i) = 0, \\ -y^r - x^r z + r_1 x^r - r_2 x^i - \delta y^i = 0, \\ -y^i - x^i z + r_1 x^i + r_2 x^r + \delta y^r = 0, \\ -b(u^2-3)z + x^r y^r + x^i y^i = 0, \\ -u|u-10| + |u+10| + z = 0. \end{cases} \tag{5}$$

From solving Eq. (5), system (4) has four none-zero equilibrium points $(0,0,0,0,9\sqrt{3}-13,\sqrt{3})$, $(0,0,0,0,-9\sqrt{3}+13,-\sqrt{3})$, $(0,0,0,0,0,(9+\sqrt{41})/2)$, $(0,0,0,0,0,(9-\sqrt{41})/2)$. In order to explore the stability and eigenvalues of the equilibrium points of the laser system, we select the equilibrium point $S\,(0,0,0,0,9\sqrt{3}-13,\sqrt{3})$ for analysis. Jacobian matrix of system (4) at S is described as

$$\boldsymbol{J} = \begin{pmatrix} -\sigma & 0 & \sigma & 0 & 0 & 0 \\ 0 & -\sigma & 0 & \sigma & 0 & 0 \\ r_1 - e & -r_2 & -1 & -\delta & 0 & 0 \\ r_2 & r_1 - e & \delta & -1 & 0 & 0 \\ 0 & 0 & 0 & 0 & 0 & -2\sqrt{3}eb \\ 0 & 0 & 0 & 0 & 1 & 2\sqrt{3}-9 \end{pmatrix},$$

where $e = 9\sqrt{3} - 13$. Corresponding characteristic equation is $a_0\lambda^6 + a_1\lambda^5 + a_2\lambda^4 + a_3\lambda^3 + a_4\lambda^2 + a_5\lambda + a_6 = 0$,

$$\begin{cases} a_0 = 1, \\ a_1 = 2\sigma - 2\sqrt{3} + 11, \\ a_2 = -2(2\sqrt{3}-9) + 4\sigma + \delta^2 + \sigma^2 - 2r_1\sigma + 2\sqrt{3}eb \\ \quad + 2e\sigma + 2(2\sqrt{3}-9)\sigma + 1, \\ a_3 = 2\sigma + 2\sigma^2 - 2r_1\sigma - (2\sqrt{3}-9)\delta^2 + 2\delta^2\sigma + 2e\sigma^2 \\ \quad - (2\sqrt{3}-9)\sigma^2 - 2r_1\sigma^2 + 4\sqrt{3}eb + 2\delta r_2\sigma \\ \quad - 2e(2\sqrt{3}-9)\sigma - (324 - 107\sqrt{3})r_1\sigma - (2\sqrt{3}-9) \\ a_4 = (395 - 220\sqrt{3})\sigma^2 + (\delta^2 - 2r_1^2 + r_2^2)\sigma^2 + 2\sqrt{3}eb \\ \quad - 2(2\sqrt{3}-9)\sigma + 8\sqrt{3}eb\sigma - (342 - 214\sqrt{3})\sigma \\ \quad + 2(2\sqrt{3}-9)r_1\sigma + 2\sqrt{3}eb\sigma^2 + 2\sqrt{3}eb\delta^2 \\ \quad - 2(2\sqrt{3}-9)\sigma\delta^2 + 2r_2\delta^2\sigma^2 + (8 - 14\sqrt{3})r_1\sigma^2 \\ \quad + 4\sqrt{3}ebr_1\sigma - 4er_1b\sigma - 2(2\sqrt{3}-9)r_2\sigma\delta, \\ a_5 = -(2\sqrt{3}-9)\sigma^2 + 4\sqrt{3}eb\sigma - (342 - 214\sqrt{3})\sigma^2 \\ \quad + 4\sqrt{3}e\sigma^2 + 2(2\sqrt{3}-9)r_1\sigma^2 - (2\sqrt{3}-9)\sigma^2\delta^2 \\ \quad - (2\sqrt{3}-9)e^2\sigma^2 - (2\sqrt{3}-9)r_1^2\sigma^2 - (2\sqrt{3}-9)r_2^2\sigma^2 \\ \quad + 4\sqrt{3}eb\sigma\delta^2 - 4\sqrt{3}(e^2)b\sigma - 2(2\sqrt{3}-9)r_2\delta\sigma^2 \\ \quad + 2e(2\sqrt{3}-9)r_1\sigma^2 + 4\sqrt{3}ebr_2\sigma\delta, \\ a_6 = 4\sqrt{3}(e^2)b\sigma^2 - 4\sqrt{3}eb\sigma^2 r_1 + 2\sqrt{3}eb\sigma^2\delta r_2 \\ \quad - 2\sqrt{3}ber_1\sigma + 2\sqrt{3}eb\delta^2\sigma^2 + 2\sqrt{3}eb\sigma^2\delta r_2. \end{cases}$$

When $r_1 = 130, \sigma = 20, \delta = 0.01, r_2 = 0.01, b = 0.01$, a_2 is less than 0, which does not meet the condition of Routh–Hurwitz stability criterion. The eigenvalues at S are given as follows: $\lambda_1 = 21.73 + 0.0096\mathrm{j}, \lambda_2 = 21.73 - 0.0096\mathrm{j}, \lambda_3 = -42.73 + 0.0004\mathrm{j}, \lambda_4 = -42.73 - 0.0004\mathrm{j}, \lambda_5 = -0.016, \lambda_6 = -5.52$. Therefore, S is an unstable saddle-focus. Similarly, the other three equilibrium points are also unstable saddle-focus.

Obviously, system (4) has symmetry because of invariance when $x^r \to -x^r, x^i \to -x^i, y^r \to -y^r, y^i \to -y^i, z \to z, u \to u$. The super volume shrinkage rate can be computed by

$$\begin{aligned} D^+V &= \frac{D^+\dot{x}^r}{D^+x^r} + \frac{D^+\dot{x}^i}{D^+x^i} + \frac{D^+\dot{y}^r}{D^+y^r} + \frac{D^+\dot{y}^i}{D^+y^i} + \frac{D^+\dot{z}}{D^+z} + \frac{D^+\dot{u}}{D^+u} \\ &= -2\sigma - 2 - b(u^2 - 3) - |u - 10| \\ &\quad -u\,\mathrm{sign}(u-10) + \mathrm{sign}(u+10). \end{aligned} \tag{6}$$

When $r_1 = 130, \sigma = 20, \delta = 0.01, r_2 = 0.01, b = 0.01$ and the initial values $(1, -1, 1, -1, 1, -1)$, the dissipation curve is shown in Fig. 3. Figure 3 shows that the dissipation remains negative, which indicates that system (4) is dissipative.

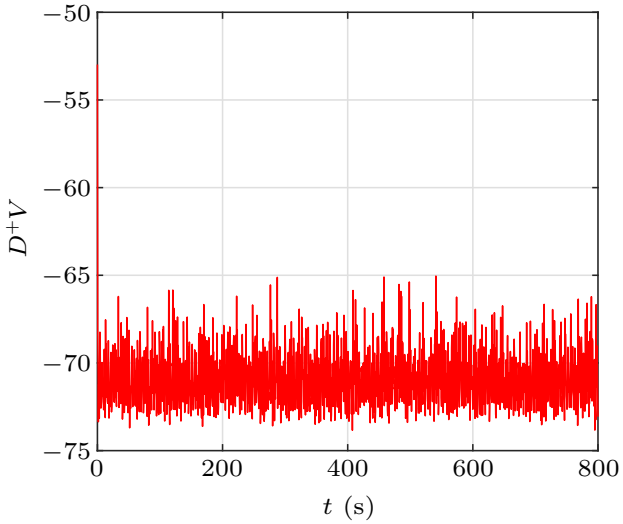


Fig. 3. The dissipation curve of system (4) with parameters $r_1 = 130$, $\sigma = 20$, $\delta = 0.01$, $r_2 = 0.01$, $b = 0.01$ and the initial values $(1, -1, 1, -1, 1, -1)$.

For parameters $r_1 = 130$, $\sigma = 20$, $\delta = 0.01$, $b = 0.01$, $r_2 = 0.01$ and the initial values $(1, -1, 1, -1, 1, -1)$, the typical orbits of system (4) are shown in Figs. 4(a) and 4(b), corresponding Lyapunov exponents are $(2.63, 0, 0, -20.99, -23.68, -28.84)$ and Kaplan–Yorke dimension is 3.125, which means chaos. The time domain waveform and power spectrum of system (4) are shown in Figs. 4(c) and 4(d), the random evolution of variable z with time and dense spikes in the power spectrum indicates system (4) is chaotic.

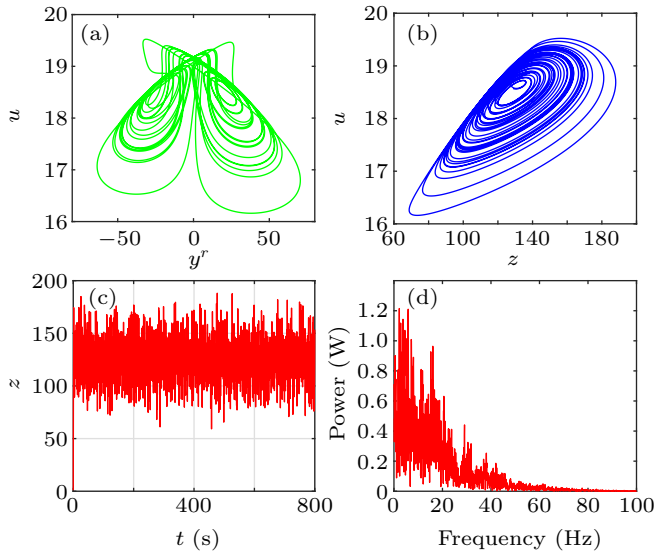


Fig. 4. Chaotic dynamics of the memristive system (4) with $r_1 = 130$, $\sigma = 20$, $\delta = 0.01$, $b = 0.01$, $r_2 = 0.01$ and the initial values $(1, -1, 1, -1, 1, -1)$. (a) The phase trajectory on y^r–u plane and (b) z–u plane; (c) time domain waveform; (d) power spectrum.

2.4. Hamilton energy for memristive complex-valued Lorenz laser system

In this section, we will seek a variable function in the phase space as the Hamilton energy function. Assuming that the Hamilton energy function of system (3) is H, H satisfies the following conditions:

$$\begin{cases} \nabla H^{\mathrm{T}} F_{\mathrm{c}}(x^r, x^i, y^r, y^i, z, u) = 0, \\ \nabla H^{\mathrm{T}} F_{\mathrm{d}}(x^r, x^i, y^r, y^i, z, u) = \dot{H} = \mathrm{d}H/\mathrm{d}t, \end{cases} \tag{7}$$

where $F_{\mathrm{c}}(x^r, x^i, y^r, y^i, z, u)$ is the conservative field, and $F_{\mathrm{d}}(x^r, x^i, y^r, y^i, z, u)$ is the dissipative field.[37] Then system (3) can be broken down into the following forms:

$$\begin{aligned} \begin{pmatrix} \dot{x}^r \\ \dot{x}^i \\ \dot{y}^r \\ \dot{y}^i \\ \dot{z} \\ \dot{u} \end{pmatrix} &= \begin{pmatrix} \sigma y^r \\ \sigma y^i \\ r_1 x^r - \delta y^i - x^r z \\ r_1 x^i + \delta y^r - x^i z \\ x^r y^r + x^i y^i - u \\ z \end{pmatrix} + \begin{pmatrix} -\sigma x^r \\ -\sigma x^i \\ -y^r - r_2 x^i \\ -y^i + r_2 x^r \\ -b(u^2 - 3)z + u \\ -u|u - 10| + |u + 10| \end{pmatrix} \\ &= F_{\mathrm{c}}(x^r, x^i, y^r, y^i, z, u) + F_{\mathrm{d}}(x^r, x^i, y^r, y^i, z, u). \end{aligned}$$

According to the criterion (7), the energy function $H(x^r, x^i, y^r, y^i, z, u)$ satisfies the following equation:

$$\begin{cases} \dfrac{\partial H}{\partial x^r}(\sigma y^r) + \dfrac{\partial H}{\partial x^i}(\sigma y^i) + \dfrac{\partial H}{\partial y^r}(r_1 x^r - \delta y^i - x^r z) + \dfrac{\partial H}{\partial y^i}(r_1 x^i + \delta y^r - x^i z) + \dfrac{\partial H}{\partial z}(x^r y^r + x^i y^i - u) + \dfrac{\partial H}{\partial u}(z) = 0, \\ \dfrac{\partial H}{\partial x^r}(-\sigma x^r) + \dfrac{\partial H}{\partial x^i}(-\sigma x^i) + \dfrac{\partial H}{\partial y^r}(-y^r - r_2 x^i) + \dfrac{\partial H}{\partial y^i}(-y^i + r_2 x^r) + \dfrac{\partial H}{\partial z}(-b(u^2 - 3)z + u) + \dfrac{\partial H}{\partial u}(-u|u - 10| + |u + 10|) = \dot{H}. \end{cases} \tag{8}$$

By solving Eq. (8), the energy function $H(x^r, x^i, y^r, y^i, z, u)$ can be obtained

$$H = \frac{1}{2}\Big(-\frac{r_1}{\sigma}(x^r)^2 - \frac{r_1}{\sigma}(x^i)^2 + (y^r)^2 + (y^i)^2 + z^2 + u^2\Big). \quad (9)$$

The Hamilton energy function H is dependent on the parameters (σ, r_1) and all variables $(x^r, x^i, y^r, y^i, z, u)$.

3. Parameters-oriented dynamical behaviors

In this section, we mainly investigate the effects of the imaginary parts of the complex-parameters r and c on the dynamical behavior of the laser system (3). Fix parameters $c = 1 - \mathrm{j}\delta$, $r = 130 + \mathrm{j}r_2$, $\sigma = 20$, $b = 0.01$ and the initial value $X_0 = (1-\mathrm{j}, 1-\mathrm{j}, 1, -1)$.

3.1. Influence of the imaginary part r_2 of the complex-parameter r

Figure 5 depicts the dynamical behaviors of the laser system (3) when parameter r_2 varies within the range $(0, 4)$. In Figs. 5(a) and 5(b), which correspond to the Lyapunov exponent spectrum and the bifurcation diagram, system (3) alternately displays chaos and quasi-periodic oscillation. When r_2 is in $(0, 1.21)$, system (3) is in a chaotic state, then when r_2 enters into $(1.21, 1.29)$, system (3) is in a quasi-periodic state; when r_2 belongs to $(1.29, 1.86)$, system (3) returns to a chaotic state; and when r_2 drops in the interval $(1.86, 4)$, system (3) goes back to quasi-period again. Typical phase trajectories of the laser system (3) with parameters r_2 in different ranges are shown in Figs. 5(c)–5(f), and the corresponding Lyapunov exponents and Kaplan–Yorke dimension are given in Table 1. When $r_2 = 0.05$ and $r_2 = 1.32$, the chaotic attractors are shown in Figs. 5(c) and 5(e), respectively. It can also be seen in Table 1 that the attractors in Figs. 5(c) and 5(e) have a positive Lyapunov exponent and fractional dimension which means chaos. The quasi-periodic attractors in Figs. 5(d) and 5(f) are at $r_2 = 1.28$ and $r_2 = 3.6$, respectively. Additionally, the two highest Lyapunov exponents are zero, which also indicates quasi-period. The Poincare cross section and Hamilton energy development of the laser system (3) are shown in Fig. 6 as r_2 varies. The poincare sections of Figs. 5(c) and 5(d) are shown in Figs. 6(a) and 6(b), respectively. The dense patches in Fig. 6(a) with fractal structures show that the attractor in Fig. 5(c) is chaotic. But the attractor in Fig. 5(d) is quasi-periodic, as evidenced by a closed curve in Fig. 6(b). The Hamilton energies of Figs. 5(c) and 5(d) are shown in

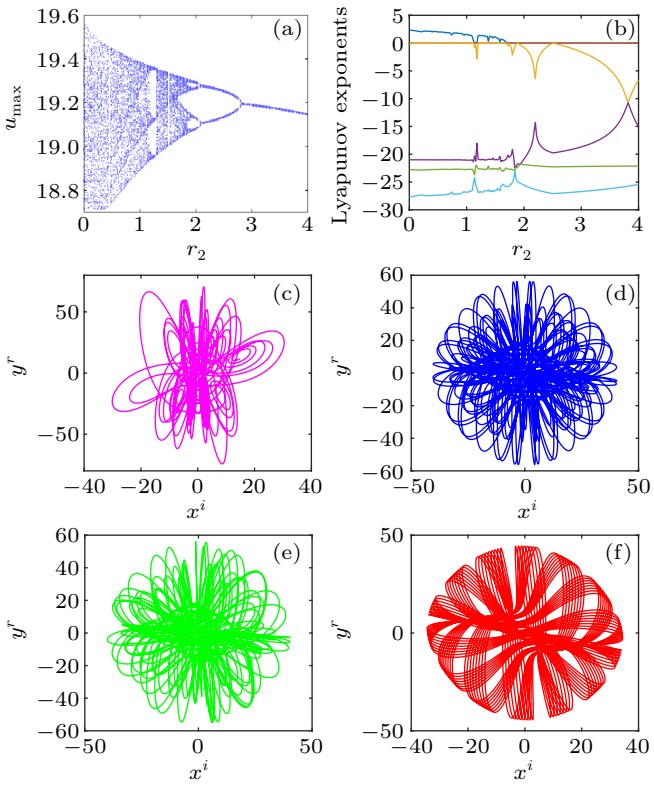


Fig. 5. Influence of r_2 on the dynamics of the laser system (3) for parameters $c = 1 - 0.01\mathrm{j}$, $r = 130 + \mathrm{j}r_2$, $\sigma = 20$, $b = 0.01$ and the initial value X_0. (a) Bifurcation diagram and (b) Lyapunov exponent spectrum with respect to r_2; the chaotic attractor on x^i–y^r plane when (c) $r_2 = 0.05$ and (e) $r_2 = 1.32$; the quasi-periodic attractor on x^i–y^r plane when (d) $r_2 = 1.28$ and (f) $r_2 = 3.6$.

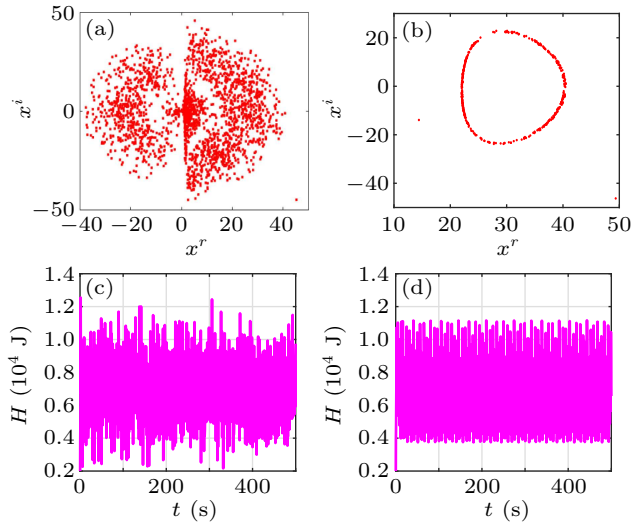


Fig. 6. Influence of r_2 on the Poincare cross section and Hamilton energy of the laser system (3) for parameters $c = 1 - 0.01\mathrm{j}$, $r = 130 + \mathrm{j}r_2$, $\sigma = 20$, $b = 0.01$ and the initial value X_0. (a) The Poincare section and (c) Hamilton energy of chaotic attractor when $r_2 = 0.05$, (b) the Poincare section and (d) Hamilton energy of quasi-periodic attractor when $r_2 = 1.28$.

Table 1. Lyapunov exponents and D_{KY} of attractors in Fig. 5.

r_2	Attractor	Figure	Lyapunov exponents	D_{KY}
0.05	chaotic	Fig. 5(c)	$(2.5466, 0, 0, -20.9969, -23.6589, -28.7728)$	3.11
1.28	quasi-periodic	Fig. 5(d)	$(0, 0, -1.2835, -19.3735, -23.5148, -26.7534)$	2
1.32	chaotic	Fig. 5(e)	$(1.5767, 0, 0, -20.9328, -23.8492, -27.7090)$	3.07
3.6	quasi-periodic	Fig. 5(f)	$(0, 0, -2.9705, -17.7945, -23.3636, -26.9422)$	2

Figs. 6(c) and 6(d), respectively. It can be seen that when the laser system (3) moves from chaos to quasi-periodic oscillation, the Hamilton energy fluctuation is reduced to a very tiny scale.

3.2. Influence of the imaginary part δ of the complex-parameter c

Figure 7 displays the dynamical behaviors of the laser system (3) when parameter δ fluctuates in the range of $(0,5)$. Figures 7(a) and 7(b) illustrate the related Lyapunov exponent spectrum and bifurcation diagram, respectively. System (3) exhibits alternately chaotic and quasi-periodic oscillations. When δ belongs to $(0,2.56)$, system (3) is in a chaotic state. When δ enters into $(2.56,2.7)$, system (3) is quasi-periodic. System (3) returns to chaos when δ drops in the interval $(2.7,3.93)$, system (3) goes back to a quasi-periodic state again when δ belongs to $(3.93,5)$. Typical phase trajectories are shown in Figs. 7(c) and 7(d) when $\delta = 0.12$ and $\delta = 4.6$, respectively. Corresponding Lyapunov exponents and Kaplan–Yorke dimension are given in Table 2. The table shows that the attractor in Fig. 7(c) is chaotic, because when $\delta = 0.12$ system (3) appears in fractional dimension and has a positive Lyapunov exponent. On account of the two largest Lyapunov exponents of the system being 0 when $\delta = 4.6$, the attractor in Fig. 7(d) is quasi-periodic. Poincare sections of Figs. 7(c) and 7(d) are shown in Figs. 8(a) and 8(b). The appearance of dense points with fractal structure in the poincare section indicates the attractor in Fig. 7(c) is chaotic, the closed curve in the poincare section confirms that the attractor in Fig. 7(d) is quasi-periodic. And according to the Hamilton energy function represented in Eq. (9), the evolution of Hamilton energy for the laser system (3) is shown in Fig. 8. Figure 8(c) is the energy of system (3) at $\delta = 0.12$, and Fig. 8(d) is at $\delta = 4.6$. When the laser system (3) is guided from chaos to quasi-periodic oscillation, the Hamilton energy fluctuation decreases to a smaller range.

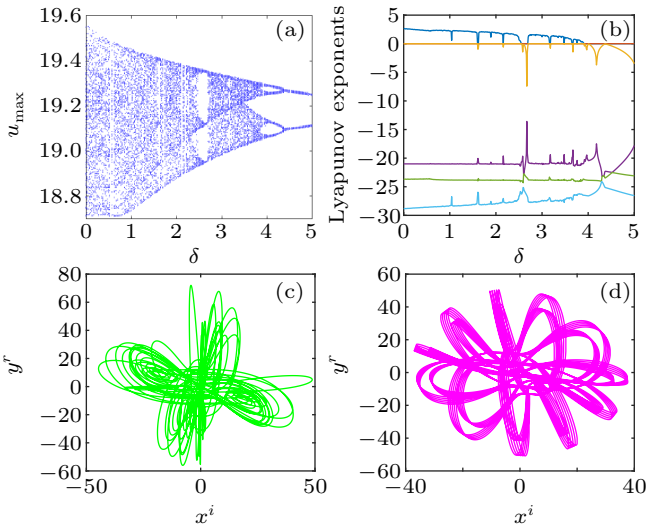


Fig. 7. Influence of δ on the dynamics of the laser system (3) for parameters $c = 1 - \mathrm{j}\delta$, $r = 130 + 0.01\mathrm{j}$, $\sigma = 20$, $b = 0.01$ and the initial value X_0. (a) Bifurcation diagram and (b) Lyapunov exponent spectrum with respect to δ; (c) the chaotic attractor on x^i–y^r plane when $\delta = 0.12$; (d) the quasi-periodic attractor on x^i–y^r plane when $\delta = 4.6$.

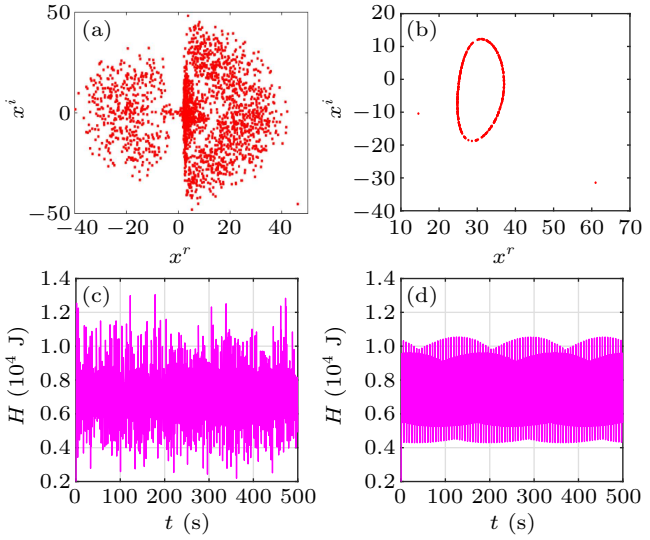


Fig. 8. Influence of δ on the Poincare cross section and Hamilton energy of the laser system (3) for parameters $c = 1 - \mathrm{j}\delta$, $r = 130 + 0.01\mathrm{j}$, $\sigma = 20$, $b = 0.01$ and the initial value X_0. (a) The Poincare section and (c) Hamilton energy of the chaotic state when $\delta = 0.12$; (b) the Poincare section and (d) Hamilton energy of the quasi-periodic state when $\delta = 4.6$.

Table 2. Lyapunov exponents and D_{KY} of attractors in Fig. 7.

δ	Attractor	Figure	Lyapunov exponents	D_{KY}
0.12	chaotic	Fig. 7(c)	$(2.5453, 0, 0, -20.9983, -23.6595, -28.7818)$	3.12
4.6	quasi-periodic	Fig. 7(d)	$(0, 0, -0.6879, -21.9242, -22.6287, -25.6850)$	2

4. Initial-values-oriented multi-stability

In this section, we investigate the effects of initial values on the dynamic behavior of the laser system (3). The symmetric structure of system (3) and the introduction of memristor (2) make the multi-stability possible. Figure 9 shows the influence of the initial value $z(0)$ on the dynamics of system (3) for parameters $\sigma = 20, r = 130 + 0.01\mathrm{j}, b = 0.01, c = 1 - 0.01\mathrm{j}$ and the initial values $(1-\mathrm{j}, 1-\mathrm{j}, z(0), -1)$. Figures 9(a) and 9(b) are the Lyapunov exponent spectrum and bifurcation diagram concerning $z(0)$, respectively. The chaotic dynamics of system (3) are almost constant and an infinite number of coexisting attractors can be discovered, which means that system (3) exhibits extreme multi-stability. Figures 9(c) and 9(d) show coexisting chaotic attractors resembling rotation in different spaces. Obviously, the chaotic dy-

namics of this type of interesting extreme multi-stability phenomena do not change.

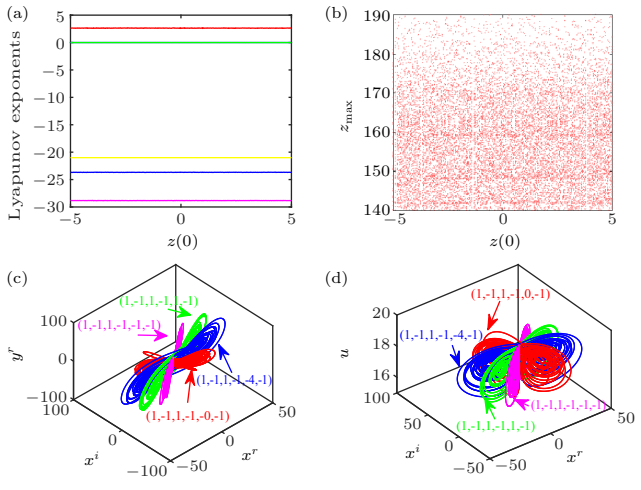


Fig. 9. Influence of initial value $z(0)$ on the laser system (3) for the initial values $(1-\mathrm{j}, 1-\mathrm{j}, z(0), -1)$ and parameters $\sigma = 20, r = 130+0.01\mathrm{j}, b = 0.01, c = 1-0.01\mathrm{j}$. (a) The Lyapunov exponent spectrum; (b) bifurcation diagram with respect to $z(0)$; coexisting chaotic attractors in (c) x^r–x^i–y^r space and (d) x^r–x^i–u space.

5. Complexity analysis

The complexity is an important index to measure the degree to which the sequence is close to the random sequence.[38,39] The higher the value of system complexity, the closer the sequence is to random sequence, and the higher the corresponding security. In this section, we compare the complexity of systems (1) and (3).

5.1. SE complexity

SE complexity is calculated by removing the DC part of the signal and combining it with the concept of Shannon entropy to calculate the capability distribution within the Fourier transform. Finally, the complexity of the sequence is obtained through normalization. When the power spectrum distribution of the sequence is more uneven, the structure of the spectrum is simpler, and the signal has an obvious oscillation rule, then the smaller the measured value of SE, the smaller the complexity; otherwise, the greater the complexity. The SE complexity of variable z of systems (1) and (3) with parameters $r = 130+0.01\mathrm{j}$, $c = 1-0.01\mathrm{j}$, $b = 0.01$ and the initial values $(1-\mathrm{j}, 1-\mathrm{j}, 1, -1)$ are shown in Fig. 10. It can be seen that

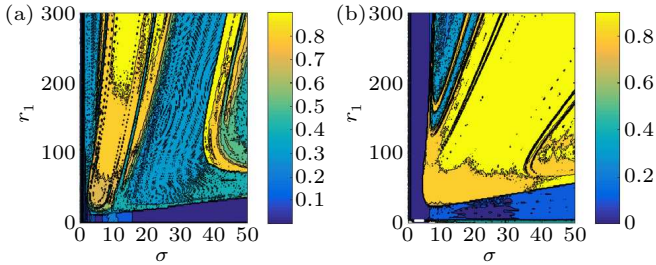


Fig. 10. The SE complexity of (a) the laser system (1) and (b) the laser system (3).

the high complexity region of the newly constructed memristive Lorenz laser system (3) is obviously larger than that of the Lorenz laser system (1).

5.2. The C_0 complexity

The C_0 complexity is to decompose the signal sequence into the regular part and irregular part and then measure the proportion of the irregular part. The larger the proportion of the irregular part in the sequence, the closer the signal is to the random sequence and the greater the complexity of the sequence. The C_0 complexity comparisons of variable x^i and variable z are shown in Fig. 11, where the blue curve is the complexity of system (1), and the red one is the complexity of the memristive laser system (3) when parameters $r = 130+0.01\mathrm{j}$, $c = 1-0.01\mathrm{j}$, $b = 0.01$ and the initial values are $(1-\mathrm{j}, 1-\mathrm{j}, 1, -1)$. From the perspective of C_0 complexity, the introduction of a locally active memristor significantly improves the complexity of system variables. Therefore, the introduction of a locally active memristor not only brings rich dynamical characteristics but also brings higher complexity, which is worthy of further study in secure communication.

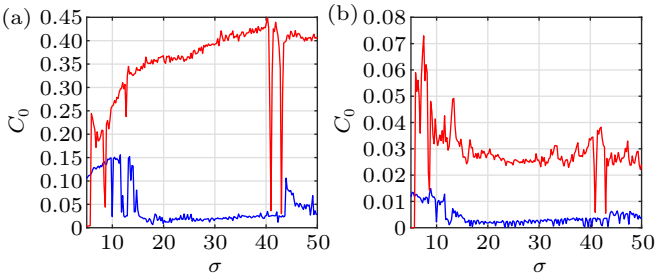


Fig. 11. The C_0 complexity of variables x^i and z of system (1) (blue) and system (3) (red). (a) C_0 complexity of variable x^i; (b) C_0 complexity of variable z.

6. Geometric control

6.1. Amplitude control

Considering that the system contains both linear and nonlinear terms, system (3) has the possibility of amplitude control. We make transformation $x \to kx$, $y \to ky$, $z \to z$, $u \to u$, the memristive complex-valued Lorenz laser system (3) becomes

$$\begin{cases} \dot{x} = \sigma(y-x), \\ \dot{y} = -cy + rx - zx, \\ \dot{z} = -b(u^2-3)z + \frac{1}{2}k^2(\bar{x}y + x\bar{y}), \\ \dot{u} = -u|u-10| + |u+10| + z. \end{cases} \tag{10}$$

The outcomes of amplitude control are displayed in Fig. 12 when the amplitude control knob k varies within the range $(0,3)$. Figure 12(a) demonstrates that while the means of x^r, x^i, y^r, y^i decrease as k increases, the means of z and u do not change. This means that the parameter k can control the amplitude of partial variables, but not the amplitude of all variables. Figure 12(b) is the Lyapunov exponent spectrum of k in the

parameter range $(0,3)$. It is observed that the Lyapunov exponents remain unchanged when k changes in $(0,3)$. This means that the introduction of parameter k can scale the amplitude of variables without changing the chaotic dynamics. The orbits diagram of the attractors under different parameter values of k are shown in Figs. 12(c) and 12(d), the amplitude changes of the phase diagram also coincide with the mean changes in Fig. 12(a).

6.2. Rotation control

Introducing the rotation matrix

$$\boldsymbol{A}=\begin{pmatrix}1&0&0&0\\0&1&0&0\\0&0&\cos\theta&\sin\theta\\0&0&-\sin\theta&\cos\theta\end{pmatrix}$$

into system (3), i.e.,

$$\begin{pmatrix}x_1\\y_1\\z_1\\u_1\end{pmatrix}=\begin{pmatrix}1&0&0&0\\0&1&0&0\\0&0&\cos\theta&\sin\theta\\0&0&-\sin\theta&\cos\theta\end{pmatrix}\begin{pmatrix}x\\y\\z\\u\end{pmatrix}.$$

And then we can obtain a rotating system as

$$\begin{cases}\dot{x}=\sigma(y-x),\\ \dot{y}=-cy+rx-x(z\cos\theta-u\sin\theta),\\ \dot{z}=\cos\theta(-b((u\cos\theta+z\sin\theta)^2-3)(z\cos\theta-u\sin\theta)+\frac{1}{2}(\bar{x}y+x\bar{y}))\\ \quad+\sin\theta(-(u\cos\theta+z\sin\theta)|(u\cos\theta+z\sin\theta)-10|+|(u\cos\theta+z\sin\theta)+10|+(z\cos\theta-u\sin\theta)),\\ \dot{u}=-\sin\theta(-b((u\cos\theta+z\sin\theta)^2-3)(z\cos\theta-u\sin\theta)+\frac{1}{2}(\bar{x}y+x\bar{y}))\\ \quad+\cos\theta(-(u\cos\theta+z\sin\theta)|(u\cos\theta+z\sin\theta)-10|+|(u\cos\theta+z\sin\theta)+10|+(z\cos\theta-u\sin\theta)).\end{cases}\tag{11}$$

When $c=1-0.01\mathrm{j}, r=130+0.01\mathrm{j}, b=0.01, \sigma=20$, and angle θ changes within the interval $(0,2\pi)$, the dynamical behavior of system (11) is shown in Fig. 13. The bifurcation diagram and Lyapunov exponent spectrum are shown in Figs. 13(a) and 13(b), respectively. It is clear that the system state does not change under the rotation transformation. The phase diagram of system (11) at different angles is shown in Fig. 13(c), and the corresponding mean value of every variable is shown in Fig. 13(d). From these two sub-figures, it can be concluded that one can control the rotating angles to make attractors appear elsewhere in the phase plane without changing the shape of the attractors. The time domain diagrams of variables z and u are shown in Figs. 13(e) and 13(f). It can be seen from the time domain diagram, by introducing a rotation matrix to rotate attractor, the amplitude of variables can be controlled to meet our needs orderly.

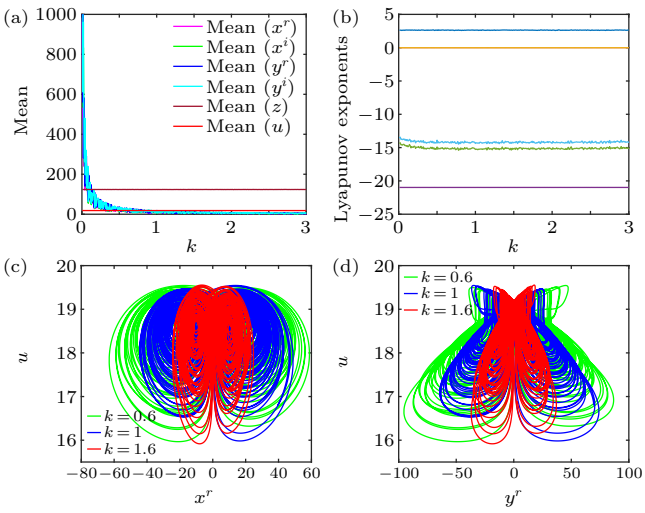


Fig. 12. Amplitude control of the memristive complex-valued Lorenz laser system (3) with parameters $c=1-0.01\mathrm{j}, r=130+0.01\mathrm{j}, b=0.01$, $\sigma=20$ and the initial values $(1-\mathrm{j},1-\mathrm{j},1,-1)$ under the parameter k. (a) The mean of every variable; (b) Lyapunov exponent spectrum with respect to k; (c) the scaled chaotic attractors on x^r–u plane and (d) y^r–u plane.

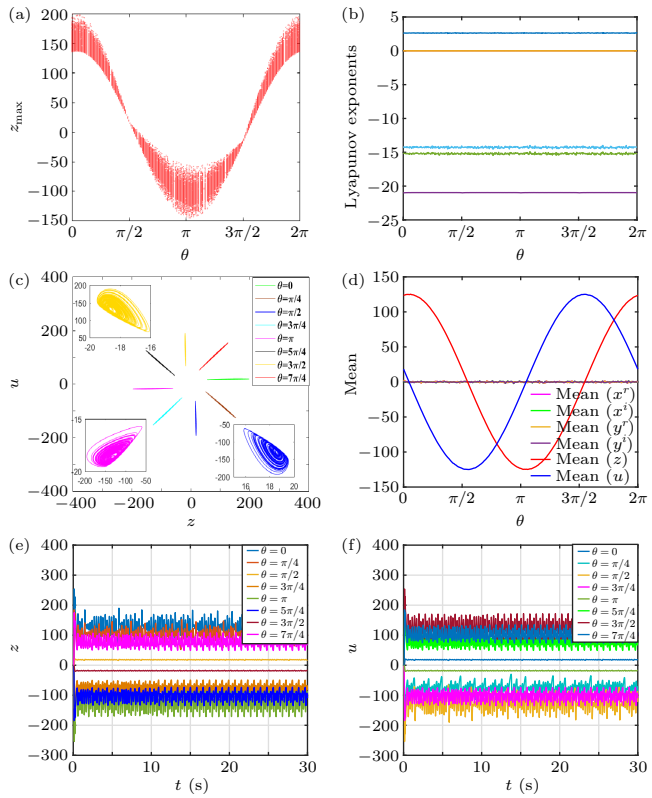


Fig. 13. The rotation control of the laser system (3) with the initial values $(1-\mathrm{j},1-\mathrm{j},1,-1)$ and parameters $c=1-0.01\mathrm{j}, r=130+0.01\mathrm{j}, b=0.01, \sigma=20$ under the parameter θ. (a) Bifurcation diagram; (b) Lyapunov exponent spectrum; (c) the rotating chaotic attractors on z–u plane; (d) the mean of every variable; (e) time domain diagram of variable z; (f) time domain diagram of variable u.

7. Digital hardware experiments

The geometric control of the memristive complex-valued Lorenz laser system is closely related to the initial values and the initial value of the memristor cannot be set in the analog circuit. To realize the analog circuit of geometric control, only by repeatedly switching on and off the analog circuit to randomly sense the required initial values. However, microcontroller-based digital circuits can treat initial values as control parameters that can be precisely preconfigured by software. In this section, a digital hardware device is designed to physically implement the proposed memristive laser system by using a microcontroller with high-performance and strong controllability, in which a microcontroller, D/A converter, and peripheral circuitry are utilized for numerically solving the memristive complex-valued laser system and generating analog voltage signal output. The ultra-performance microcontroller STM32H743IIT6 with Cortex-M4 core realizes the presented memristive laser system, and the D/A converter DAC8563 provides two-channel analog voltage sequences. After the development board is powered on, the digital oscilloscope captures the phase plane trajectories. Chaotic oscillation, amplitude control, and rotation control are experimentally observed, which are used to validate the numerical ones. To realize the digitization of the laser system (3), the fourth-order Runge–Kutta algorithm is used to obtain the discrete-time model as follows:

$$\begin{cases} x_{n+1} = x_n + \dfrac{h\,(k_{x,1}+2k_{x,2}+2k_{x,3}+k_{x,4})}{6}, \\ y_{n+1} = y_n + \dfrac{h\,(k_{y,1}+2k_{y,2}+2k_{y,3}+k_{y,4})}{6}, \\ z_{n+1} = z_n + \dfrac{h\,(k_{z,1}+2k_{z,2}+2k_{z,3}+k_{z,4})}{6}, \\ u_{n+1} = u_n + \dfrac{h\,(k_{u,1}+2k_{u,2}+2k_{u,3}+k_{u,4})}{6}, \end{cases} \tag{12}$$

where h is the sampling interval and n is the iterations. And

$$\begin{aligned}
k_{x,1} &= \sigma\,(y_n - x_n)\,, \\
k_{y,1} &= -cy_n + rx_n - z_n x_n, \\
k_{z,1} &= -b(u_n^2 - 3)z_n + \frac{1}{2}\,(\overline{x_n}y_n + x_n\overline{y_n})\,, \\
k_{u,1} &= -u_n\,|u_n - 10| + |u_n + 10| + z_n, \\
k_{x,2} &= \sigma((y_n + 0.5hk_{y,1}) - (x_n + 0.5hk_{x,1})), \\
k_{y,2} &= -c(y_n + 0.5hk_{y,1}) + r(x_n + 0.5hk_{x,1}) - (z_n + 0.5hk_{z,1})(x_n + 0.5hk_{x,1}), \\
k_{z,2} &= -b(((u_n + 0.5hk_{u,1})^2) - 3)(z_n + 0.5hk_{z,1}) + \frac{1}{2}\overline{(x_n + 0.5hk_{x,1})}(y_n + 0.5hk_{y,1}) + (x_n + 0.5hk_{x,1})\overline{(y_n + 0.5hk_{y,1})}), \\
k_{u,2} &= -(u_n + 0.5hk_{u,1})|(u_n + 0.5hk_{u,1}) - 10| + |(u_n + 0.5hk_{u,1}) + 10| + (z_n + 0.5hk_{z,1}), \\
k_{x,3} &= \sigma((y_n + 0.5hk_{y,2}) - (x_n + 0.5hk_{x,2})), \\
k_{y,3} &= -c(y_n + 0.5hk_{y,2}) + r(x_n + 0.5hk_{x,2}) - (z_n + 0.5hk_{z,2})(x_n + 0.5hk_{x,2}), \\
k_{z,3} &= -b(((u_n + 0.5hk_{u,2})^2) - 3)(z_n + 0.5hk_{z,2}) + \frac{1}{2}(\overline{(x_n + 0.5hk_{x,1})}(y_n + 0.5hk_{y,2}) + (x_n + 0.5hk_{x,1})\overline{(y_n + 0.5hk_{y,2})}), \\
k_{u,3} &= -(u_n + 0.5hk_{u,2})|(u_n + 0.5hk_{u,2}) - 10| + |(u_n + 0.5hk_{u,2}) + 10| + (z_n + 0.5hk_{z,2}), \\
k_{x,4} &= \sigma\,((y_n + hk_{y,3}) - (x_n + hk_{x,3}))\,, \\
k_{y,4} &= -c(y_n + hk_{y,3}) + r(x_n + hk_{x,3}) - (z_n + hk_{z,3})(x_n + hk_{x,3}), \\
k_{z,4} &= -b(((u_n + hk_{u,3})^2) - 3)(z_n + hk_{z,3}) + \frac{1}{2}(\overline{(x_n + hk_{x,1})}(y_n + hk_{y,3}) + (x_n + hk_{x,1})\overline{(y_n + hk_{y,3})}), \\
k_{u,4} &= -(u_n + hk_{u,3})\,|(u_n + hk_{u,3}) - 10| + |(u_n + hk_{u,3}) + 10| + (z_n + hk_{z,3}).
\end{aligned}$$

Using the discrete time model, the software code of the memristive laser system is written in C language and downloaded to the microcontroller. The system parameters and initial values are preloaded to the hardware device. After running the software, an analog voltage sequence can be generated. The captured phase plane of chaotic oscillation for the digitally circuit-implemented memristive complex-valued Lorenz laser model is shown in Fig. 14, where $c = 1 - 0.01\mathrm{j}, r = 130 + 0.01\mathrm{j}, b = 0.01, \sigma = 20, h = 0.001$ and the initial values $(x_1(0), y_1(0), z_1(0), u_1(0)) = (1 - \mathrm{j}, 1 - \mathrm{j}, 1, -1)$. Clearly, the phase trajectories captured by oscilloscope are consistent with the MATLAB numerical simulation results.

The same discretization method as system (12) is adopted to discretize systems (10) and (11) to obtain digital circuit results of geometric control as shown in Fig. 15, where appropriate zooming and bias are applied for better visual effects. Figure 15(a) shows the captured orbits for amplitude control on y^r–u plane when $c = 1-0.01\mathrm{j}$, $r = 130+0.01\mathrm{j}$, $b = 0.01$, $\sigma = 20$, $k = (0.6, 1, 1.6)$ and the initial values $(x_1(0), y_1(0), z_1(0), u_1(0)) = (k-k\mathrm{j}, k-k\mathrm{j}, 1, -1)$. Figure 15(b) shows digital circuit result of rotation control on z–u plane when $c = 1-0.01\mathrm{j}$, $r = 130+0.01\mathrm{j}$, $b = 0.01$, $\sigma = 20$, $\theta = (0, \pi/4, \pi/2, 3\pi/4, \pi, 5\pi/4, 3\pi/2, 7\pi/4)$ and the initial values $(x_1(0), y_1(0), z_1(0), u_1(0)) = (1-\mathrm{j}, 1-\mathrm{j}, \cos\theta - \sin\theta, -\cos\theta - \sin\theta)$. The experimental results shown in Figs. 14 and 15 are consistent with the numerical ones in Figs. 4, 12 and 13, indicating the correctness and feasibility of the digitally circuit-implemented memristive complex-valued laser system (3).

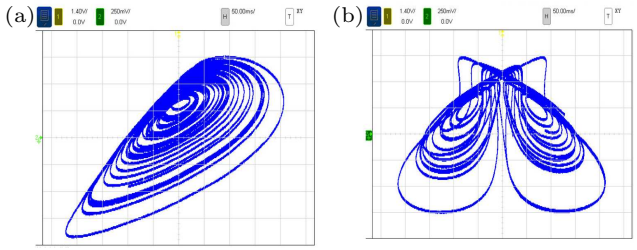


Fig. 14. Experimental phase portraits of chaotic attractors in Fig. 4 on (a) z–u plane and (b) y^r–u plane.

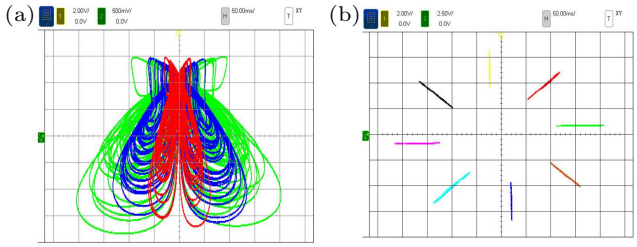


Fig. 15. Experimental phase portraits of geometric control in Figs. 12 and 13. (a) Amplitude control for $k = (0.6, 1, 1.6)$ on y^r–u plane; (b) rotation control for $\theta = (0, \pi/4, \pi/2, 3\pi/4, \pi, 5\pi/4, 3\pi/2, 7\pi/4)$ on z–u plane.

8. Conclusion

We design a memristive complex-valued laser system and study its dynamics, geometric control, and digital hardware implementation. Firstly, we study the effects of the imaginary parts of the complex-parameters on its dynamics and discover chaotic and quasi-periodic oscillations. Initial-values-associated multi-stability is also explored, coexisting attractors resembling rotations with the same Lyapunov exponents are discovered. In addition, we compare the complexity of the laser system with and without a locally active memristor and find that the introduction of a memristor increases the complexity of the laser system. Moreover, geometric control methods including amplitude and rotation control are proposed to revise the chaotic signal of the laser system. The amplitude control adjusts the size of chaotic attractors by introducing a constant, while the rotation control modulates the amplitude and offset of chaotic attractors at the same time by introducing a rotation angle. Through the analysis of the Lyapunov exponent spectrum and time domain diagram, it can be seen that the amplitude and offset of the chaotic signal can be modified without changing the chaotic dynamics. In addition, a digital circuit is constructed to physically realize the memristive complex-valued Lorenz laser system using an ultra-low power microcontroller, and the hardware experiment results are captured, which perfectly verifies the numerical simulation. It is worth mentioning that the digital hardware realization of geometric control over the complex field is completed for the first time. Further research is deserved to realize rotation control of higher dimensions, explore the practical applications of geometric control of chaos in secure communication, and apply memristive laser neurons to replace neuromorphic devices in the brain.

Acknowledgments

Project supported by the National Natural Science Foundation of China (Grant No. 61773010) and Taishan Scholar Foundation of Shandong Province of China (Grant No. ts20190938).

References

[1] Maiman T H 1960 *Nature* **187** 493
[2] Wang J Y, Mou J, Yan H Z, Liu X C, Ma Y J and Cao Y H 2021 *Eur. Phys. J. Plus* **136** 1112
[3] Chai L, Liu J, Chen G R and Zhao X 2021 *Sci. China Technol. Sci.* **64** 2729
[4] Ma C G, Banerjee S, Xiong L, Liu T M, Han X T and Mou J 2021 *Chin. Phys. B* **30** 120504
[5] Zhao X, Liu J, Mou J, Ma C G and Yang F F 2020 *Eur. Phys. J. Plus* **135** 1
[6] Alexander N P, Ricardo S E, Rider J R, Guillermo H C, Hugo G L and Victor B K 2013 *Sensors* **13** 17322
[7] Schemmel J, Bruderle D, Grubl A, Hock M, Meier K and Millner S 2010 *IEEE International Symposium on Circuits and Systems*, May 30–June 02, 2010, Paris, France, p. 1947
[8] Merolla P A, Arthur J V, Alvarez-Icaza R, Cassidy A S, Sawada J, Akopyan F, Jackson B L, Imam N, Guo C, Nakamura Y, Brezzo B, Vo I, Esser S K, Appuswamy R, Taba B, Amir A, Flickner M D, Risk W P, Manohar R and Modha D S 2014 *Science* **345** 668
[9] Turconi M, Garbin B, Feyereisen M, Giudici M and Barland S 2013 *Phys. Rev. E* **88** 022923
[10] Al-Naimee K, Marino F, Ciszak M, Abdalah S F, Meucci R and Arecchi F T 2010 *Eur. Phys. J. D* **58** 187
[11] Li Y, Chen Z Q, Yuan M F and Cang S J 2022 *Chin. Phys. B* **31** 060503
[12] Toomey J P, Nichkawde C, Kane D M, Schires K, Henning I D, Hurtado A and Adams M J 2012 *Opt. Express* **20** 10256
[13] Coomans W, Gelens L, Beri S, Danckaert J and Van der Sande G 2011 *Phys. Rev. E* **84** 036209
[14] Nahmias M A, Tait A N, Tolias L, Chang M P, Lima T F, Shastri B J and Prucnal P R 2016 *Appl. Phys. Lett.* **108** 151106
[15] Scher S and Messori G 2019 *Nonlinear Process. Geophys.* **26** 381
[16] Zhang L 2017 *IEEE 30th Canadian Conference on Electrical and Computer Engineering*, April 30–May 03, 2017, Windsor, Canada, p. 1
[17] Zhang F F, Gao R and Liu J 2021 *Chin. Phys. B* **30** 080503
[18] Jin M X, Sun K H and He S B 2023 *Chin. Phys. B* **32** 060501
[19] Zhang X T, Liu J, Wang D and Liu H J 2023 *Nonlinear Dyn.* **111** 6395

[20] Zhang H, Gu M, Jiang X D, Thompson J, Cai H, Paesani S, Santagati R, Laing A, Zhang Y, Yung M H, Shi Y Z, Muhammad F K, Lo G Q, Luo X S, Dong B, Kwong D L, Kwek L C and Liu A Q 2021 *Nat. Commun.* **12** 457
[21] Chua L 1971 *IEEE Trans. Circuit Theory* **18** 507
[22] Ma X J, Mou J, Xiong L, Banerjee S, Cao Y H and Wang J Y 2021 *Chaos Solitons Fractals* **152** 111363
[23] Cheng Y Z, Min F H, Rui Z and Zhang L 2021 *Chin. Phys. B* **30** 120502
[24] Bao H, Hua M J, Ma J, Chen M and Bao B C 2022 *IEEE Trans. Ind. Electron.* **70** 10526
[25] Dou G, Dou M L, Liu R Y and Guo M 2021 *Chin. Phys. B* **30** 078401
[26] Min F H and Rui Z 2022 *Chaos* **32** 103117
[27] Yang Z L, Liang D, Ding D W, Hu Y B and Li H 2021 *Chin. Phys. B* **30** 120515
[28] Li C B, Thio W J C, Sprott J C, Zhang R X and Lu T A 2017 *Chin. Phys. B* **26** 120501
[29] Bao H, Chen M, Wu H G and Bao B C 2020 *Sci. China Technol. Sci.* **63** 603
[30] Chen C J and Min F H 2022 *Eur. Phys. J. Spec. Top.* **231** 2979
[31] Korkmaz N 2021 *Neural Process. Lett.* **53** 3877
[32] Wang H X, Cai G L, Miao S and Tian L X 2010 *Chin. Phys. B* **19** 030509
[33] Li C B, Sprott J C and Yuan Z 2015 *Int. J. Bifurcat. Chaos* **25** 1530025
[34] Jiang Y C, Li C B, Zhang C, Zhao Y B and Zang H Y 2021 *IEEE Trans. Circuits Syst.* **68** 4935
[35] Ma X, Li C B, Li Y N, Bi L Q and Qi Z Y 2022 *Eur. Phys. J. Plus* **137** 542
[36] Sayed W S, Radwan A G, Elnawawy M, Orabi H, Sagahyroon A, Aloul F, Elwakil A S, Fahmy H A and El-Sedeek A 2019 *Circuits, Syst., Signal Process.* **38** 4890
[37] Song X L, Jin W Y and Ma J 2015 *Chin. Phys. B* **24** 128710
[38] He S B, Sun K H and Zhu C X 2013 *Chin. Phys. B* **22** 050506
[39] Sun K H, He S B, Zhu C X and He Y 2013 *Acta Electon. Sinica* **41** 1765 (in Chinese)